ADVANCED ENERGY MATERIALS
www.advenergymat.de

Lead-Free Perovskite-Inspired Absorbers for Indoor Photovoltaics

Yueheng Peng, Tahmida N. Huq, Jianjun Mei, Luis Portilla, Robert A. Jagt, Luigi G. Occhipinti, Judith L. MacManus-Driscoll, Robert L. Z. Hoye, and Vincenzo Pecunia**

With the exponential rise in the market value and number of devices part of the Internet of Things (IoT), the demand for indoor photovoltaics (IPV) to power autonomous devices is predicted to rapidly increase. Lead-free perovskite-inspired materials (PIMs) have recently attracted significant attention in photovoltaics research, due to the similarity of their electronic structure to high-performance lead-halide perovskites, but without the same toxicity limitations. However, the capability of PIMs for indoor light harvesting has not yet been considered. Herein, two exemplar PIMs, BiOI and $Cs_3Sb_2Cl_xI_{9-x}$ are examined. It is shown that while their bandgaps are too wide for single-junction solar cells, they are close to the optimum for indoor light harvesting. As a result, while BiOI and $Cs_3Sb_2Cl_xI_{9-x}$ devices are only circa 1%-efficient under 1-sun illumination, their efficiencies increase to 4–5% under indoor illumination. These efficiencies are within the range of reported values for hydrogenated amorphous silicon, i.e., the industry standard for IPV. It is demonstrated that such performance levels are already sufficient for millimeter-scale PIM devices to power thin-film-transistor circuits. Intensity-dependent and optical loss analyses show that future improvements in efficiency are possible. Furthermore, calculations of the optically limited efficiency of these and other low-toxicity PIMs reveal their considerable potential for IPV, thus encouraging future efforts for their exploration for powering IoT devices.

1. Introduction

With the emergence of Big Data and the Internet of Things (IoT), the demand for self-powered wireless devices (e.g., smart sensors for health and wellness monitoring, and for smart buildings and smart packaging) has substantially increased over the past few years.[1–6] Self-powered devices are expected to play an important role in enabling the growth of the IoT ecosystem to fulfil its future potential in terms of the number of devices and complexity, in which battery-powered devices alone are no longer expected to be practical in all cases.[7–9] A significant proportion of these wireless devices are deployed in indoor environments where varying light intensities and spectra are present, for which efficient and reliable indoor photovoltaics (IPV) would be attractive as a power supply. Generally, the intensity of indoor light sources is approximately three orders of magnitude lower than the standard terrestrial outdoor AM 1.5G solar spectrum. The illuminance of fluorescent light (FL) sources and white light emitting diodes (WLED) commonly found in residential and commercial buildings is in the range of 200–1000 lux.[10] The corresponding irradiance is approximately 50–300 μW cm^{-2}, with spectra spanning predominantly over the visible wavelength range ($400 \lesssim \lambda \lesssim 700$ nm).[11–13] As a result, although commercial crystalline silicon solar cells are suitable for harvesting terrestrial solar radiation, their bandgaps (1.12 eV) are too narrow for optimal harvesting of indoor lighting.[14] Furthermore, crystalline silicon solar cells suffer from significant Shockley-Read-Hall recombination under low light conditions.[15] Therefore, alternative absorbers with wider bandgaps are needed for IPV applications, and the technologies explored to date are based on hydrogenated amorphous silicon (a-Si:H), dye-sensitized solar cells, lead-halide perovskites and organic semiconductors.[16–19]

Hydrogenated amorphous silicon has become the industry standard for IPV because its efficiency under indoor illumination, ranging from 4.4% to 9.2%, is adequate for typical electronic devices powered by photovoltaics.[15,20–23] Among the emerging absorbers, lead-halide perovskites have been identified as particularly promising for IPV owing to their ability to achieve excellent optoelectronic properties (e.g., long diffusion lengths >1 μm) when grown by low-cost, facile methods.[24–29] Lead-halide perovskite IPV with power conversion efficiencies

Y. Peng, J. Mei, Dr. L. Portilla, Prof. V. Pecunia
Jiangsu Key Laboratory for Carbon-Based Functional Materials & Devices
Institute of Functional Nano & Soft Materials (FUNSOM)
Joint International Research Laboratory of Carbon-Based Functional Materials and Devices
Soochow University
199 Ren'ai Road, Suzhou, Jiangsu 215123, China
E-mail: vp293@suda.edu.cn

T. N. Huq, R. A. Jagt, Prof. J. L. MacManus-Driscoll
Department of Materials Science and Metallurgy
University of Cambridge
27 Charles Babbage Road, Cambridge CB3 0FS, UK

Dr. L. G. Occhipinti
Department of Engineering
University of Cambridge
9 J J Thomson Avenue, Cambridge CB3 0FA, UK

Dr. R. L. Z. Hoye
Department of Materials
Imperial College London
Exhibition Road, London SW7 2AZ, UK
E-mail: r.hoye@imperial.ac.uk

The ORCID identification number(s) for the author(s) of this article can be found under https://doi.org/10.1002/aenm.202002761.

DOI: 10.1002/aenm.202002761

of 36% under low-intensity indoor lighting have recently been demonstrated.[30] Despite their attractive performance, the use of lead-halide perovskites raises toxicity concerns. Although the lead concentration in lead-halide perovskites is lower than in natural soil, there is evidence that the highly-soluble lead content of lead-halide perovskites is ten times more bioavailable.[31,32] While the challenges of lead-containing compounds in outdoor solar applications are mostly downstream (e.g., recycling and disposal of cells at their end of life), the use of lead-halide perovskites in an indoor environment poses significantly higher risks.[33] In an indoor setting, the encapsulation layer would be the only barrier between the human end-user and the lead contained within the perovskite device, which increases the potential for lead exposure in case of damage to the device.[7,34] Moreover, the use of lead-halide perovskites to power wearable electronics and other indoor IoT devices faces regulatory challenges (e.g., the limit of 0.1 wt% Pb content set by the EU Restriction of Hazardous Substances (RoHS) directive).[35] Furthermore, lead-iodide based perovskites (e.g., methylammonium lead iodide) have a bandgap of approximately 1.6 eV (depending on the A-site cation), which is below the optimal bandgap for indoor light harvesting (1.9 eV).[36] Alloying with ≈70% bromide in place of iodide is needed to raise the bandgap to 1.9 eV, but the resulting materials are not photostable. Indeed, it has been shown that illuminating these mixed iodide-bromide perovskites with 15 mW cm^{-2} visible light for <10 min results in phase-separation and the bandgap red-shifting and settling at 1.68 eV.[36]

In the broader photovoltaics research landscape, investigators have been actively searching for lead-free perovskite-inspired materials (PIMs) with the aim of mitigating the toxicity challenges of lead-halide perovskites.[37] However, this effort has been primarily aimed at outdoor solar harvesting,[37–41] while the potential of PIMs for IPV has been unexplored to date. Among lead-free perovskite-inspired absorbers, halides and chalcohalides based on Bi^{3+} and Sb^{3+} have attracted a considerable amount of attention due to the similarity of their electronic structure to that of lead-halide perovskites, namely the s–p hybridization in the valence band and the antibonding-to-antibonding orbital transition across the bandgap.[42] Bismuth and antimony are also substantially less toxic than lead, and are sufficiently abundant for large-scale commercialization.[43–45] In devices, bismuth- and antimony-based absorbers have recently demonstrated promising performance under AM 1.5G illumination,[40,46] but have yet to reach levels comparable to their lead-halide counterparts.[44] An important limitation they face in outdoor solar harvesting is their wide bandgap of ≈2 eV. However, such bandgap values are in fact optimal for indoor light harvesting owing to the spectra of indoor light sources being blue-shifted compared to the AM 1.5G spectrum.[7,14,15] Furthermore, PIMs absorbing in the visible light spectrum come in aesthetically appealing colors, thus addressing the need for photovoltaics that can also carry out a decorative function when deployed in the objects and environments of our daily lives.[32,45,47–52] Additionally, antimony- and bismuth-based PIMs can be synthesized using techniques that are compatible with low-cost flexible plastic substrates, thereby pointing to their integration into a wide range of IoT devices.[53–56]

In this study we aim to shed light on the indoor photovoltaic capabilities and potential of lead-free perovskite-inspired absorbers. Specifically, we first investigate two exemplar absorbers, and subsequently assess the significance of our findings in the broader PIM landscape. The exemplar materials we first study in detail are bismuth oxyiodide (BiOI) and the defect-ordered perovskite cesium antimony chloride-iodide ($Cs_3Sb_2Cl_xI_{9-x}$). Both materials have bandgaps close to 1.9 eV without requiring any further alloying. Critically, while many Bi^{3+} and Sb^{3+} PIMs have a 0D crystal or electronic structure, BiOI and $Cs_3Sb_2Cl_xI_{9-x}$ have layered (2D) structures.[44,46,47,50] This allows efficient charge transport within the covalently linked planes, such that >60% external quantum efficiencies could be achieved in devices.[32,45,56] Herein, we investigate the photovoltaic performance of BiOI and $Cs_3Sb_2Cl_xI_{9-x}$ devices under FL and WLED illumination, as compared to AM 1.5G radiation, and assess whether their performance is sufficient to power thin-film-transistor (TFT) circuits for digital processing. Furthermore, we perform intensity-dependent measurements and optical loss analyses to determine the pathways for achieving future increases in efficiency. Finally, we estimate the efficiency in the radiative limit and the spectroscopically limited maximum efficiency (SLME) of a range of perovskite-inspired absorbers under AM 1.5G and indoor light conditions in order to demonstrate the potential of these materials for indoor light harvesting applications, and make recommendations for PIMs that should be investigated further in the future.

2. Results and Discussion

2.1. BiOI and $Cs_3Sb_2Cl_xI_{9-x}$ Photovoltaic Devices

Thin films of BiOI and $Cs_3Sb_2Cl_xI_{9-x}$ were grown by thermal chemical vapor deposition (t-CVD) and solution processing, respectively, using our previously established routes.[45,56] BiOI has a layered structure, with a tetragonal unit cell (space group *P4/nmm*, no. 129), as shown in **Figure 1**a. $Cs_3Sb_2I_9$, on the other hand, can adopt either a 0D structure (space group $P6_3/mmc$, no. 194) or 2D structure (space group $P\bar{3}m1$, no. 164).[56] As explained in our previous work,[56] the 2D phase can be stabilized by introducing Cl (Figure 1a). Stabilizing the layered phase is important for improving the charge transport properties of the material.[56] X-ray diffraction (XRD) patterns of the thin films grown show both materials to be phase pure with the layered structures (Figure 1b). The BiOI grown on NiO_x/ITO had a compact morphology (Figure 1c), with a film thickness of ≈700 nm and grains of comparable size, which adopt a {012} preferred orientation. This preferred orientation is favorable for charge extraction in a vertically structured device.[57] $Cs_3Sb_2Cl_xI_{9-x}$ had smaller grains (≈250 nm in size) with a less-dense morphology when grown on mesoporous TiO_2/FTO, which we nonetheless found to allow devices with high photoconversion efficiency.[56]

Critically, both BiOI and $Cs_3Sb_2Cl_xI_{9-x}$ have bandgaps close to the optimum value of 1.9 eV for IPV applications (1.93 eV for BiOI and 1.95 eV for $Cs_3Sb_2Cl_xI_{9-x}$), as shown in our previous works.[45,56] Both materials demonstrated room-temperature photoluminescence (PL), as shown in Figure S1

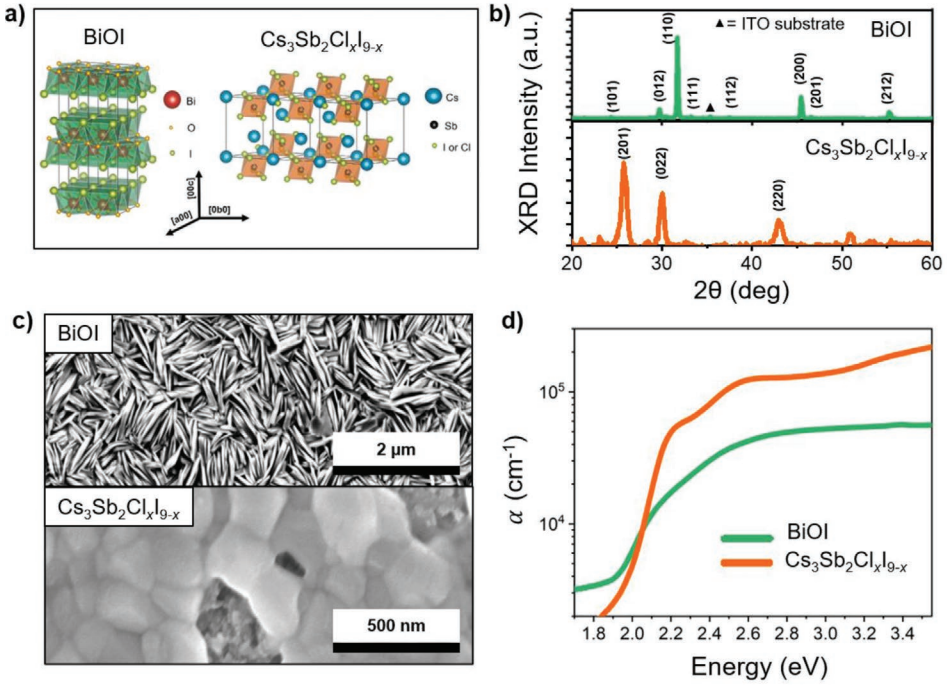

Figure 1. Structural and optical properties of BiOI and $Cs_3Sb_2Cl_xI_{9-x}$ thin films. a) Crystal structure, b) X-ray diffraction patterns, c) scanning electron microscopy images of the absorbers deposited onto ITO/NiO_x (BiOI) or FTO/TiO_2/m-TiO_2 ($Cs_3Sb_2Cl_xI_{9-x}$), and d) absorption coefficients.

(Supporting Information). The PL peak for $Cs_3Sb_2Cl_xI_{9-x}$ was centered at 1.96 ± 0.01 eV, which is consistent with the optical bandgap. The PL for BiOI, on the other hand, was centered at 1.77 ± 0.01 eV. We are currently investigating the origin of this Stokes shift and going into this in detail is beyond the scope of the present work. We investigated the photostability of the materials by repeatedly measuring the PL spectrum over the course of 30 min illumination with a pulsed 3.1 eV laser with a fluence of 14 μJ cm^{-2} pulse^{-1}. No shift in the PL peak occurred in either material (Figure S1, Supporting Information), showing the materials to be photostable under the excitation conditions used.

We constructed devices from both materials using the architectures that have yielded the highest efficiencies under 1-sun illumination (**Figure 2**a,b, with device stacks shown in Figure S2, Supporting Information).[45,56] The external quantum efficiency (EQE) spectra of both devices demonstrate significantly greater overlap with the FL and WLED spectra than with the AM 1.5G spectrum (Figure 2c). This points to the considerably greater potential of these materials for IPV applications than for outdoor solar harvesting.

The current density–voltage (*J*–*V*) characteristics of BiOI and $Cs_3Sb_2Cl_xI_{9-x}$ devices were measured under AM 1.5G, FL (1000 lux), and WLED (1000 lux) illumination (Figure 2d–f; see **Table 1** for the corresponding performance parameters). As shown in Figure 2e, devices based on BiOI and $Cs_3Sb_2Cl_xI_{9-x}$ have a power conversion efficiency (PCE) of 0.9% and 1.2% under AM 1.5G illumination respectively, which is in agreement with the median efficiency of these materials in prior reports.[45,56,58] However, under FL and WLED illumination, the PCE values increased to the range of 4–5%, peaking at 4.4% for BiOI and 4.9% for $Cs_3Sb_2Cl_xI_{9-x}$ under FL lighting (Figure 2d,f). These PCEs have already entered the range of efficiencies reported for commercial a-Si:H IPV (4.4–9.2%).[15,21–23] This confirms the appeal of these lead-free absorbers for IPV applications. Importantly, their efficiency values under indoor light sources correspond to a fourfold increase with respect to their PCE under 1-sun illumination, reflecting the closer match of their absorption spectra with indoor light sources.

The IPV performance of both BiOI and $Cs_3Sb_2Cl_xI_{9-x}$ devices without encapsulation was found to be stable over a 5 month period, during which they were kept in a N_2-filled environment that contained >1000 ppm oxygen and >500 ppm H_2O (stability curves shown in Figures S3 and S4 (Supporting Information); the distribution of the photovoltaic parameters is provided in Figure S5, Supporting Information). These conditions are similar to those that might be expected for encapsulated devices stored in ambient air.[59] In fact, the devices improved in performance after 5 months of storage in this environment, in which the PCE of $Cs_3Sb_2Cl_xI_{9-x}$ more than doubled, increasing from 2.3% to 4.9% under FL illumination, and from 1.9% to 4.4% under WLED illumination. In the case of BiOI, the PCE increased from 2.4% to 4.0% under FL illumination, and remained stable at ≈3.4% under WLED illumination before and after 5 months of storage. In particular, the PCE improvement of the BiOI device under FL lighting can be primarily traced to an improved J_{sc}—which increased from 46 to 61 μA cm^{-2}—and fill factor—which increased from 32% to 45% (see Figure S3, Supporting Information). In contrast, the $Cs_3Sb_2I_xCl_{9-x}$ device manifested an appreciable improvement mainly in the J_{sc} and V_{oc}, which increased from 50 to 82 μA cm^{-2} and from 0.41 to 0.49 V, respectively (see Figure S4, Supporting Information). The mechanism through which the improvement occurs is unclear, but, based on related findings

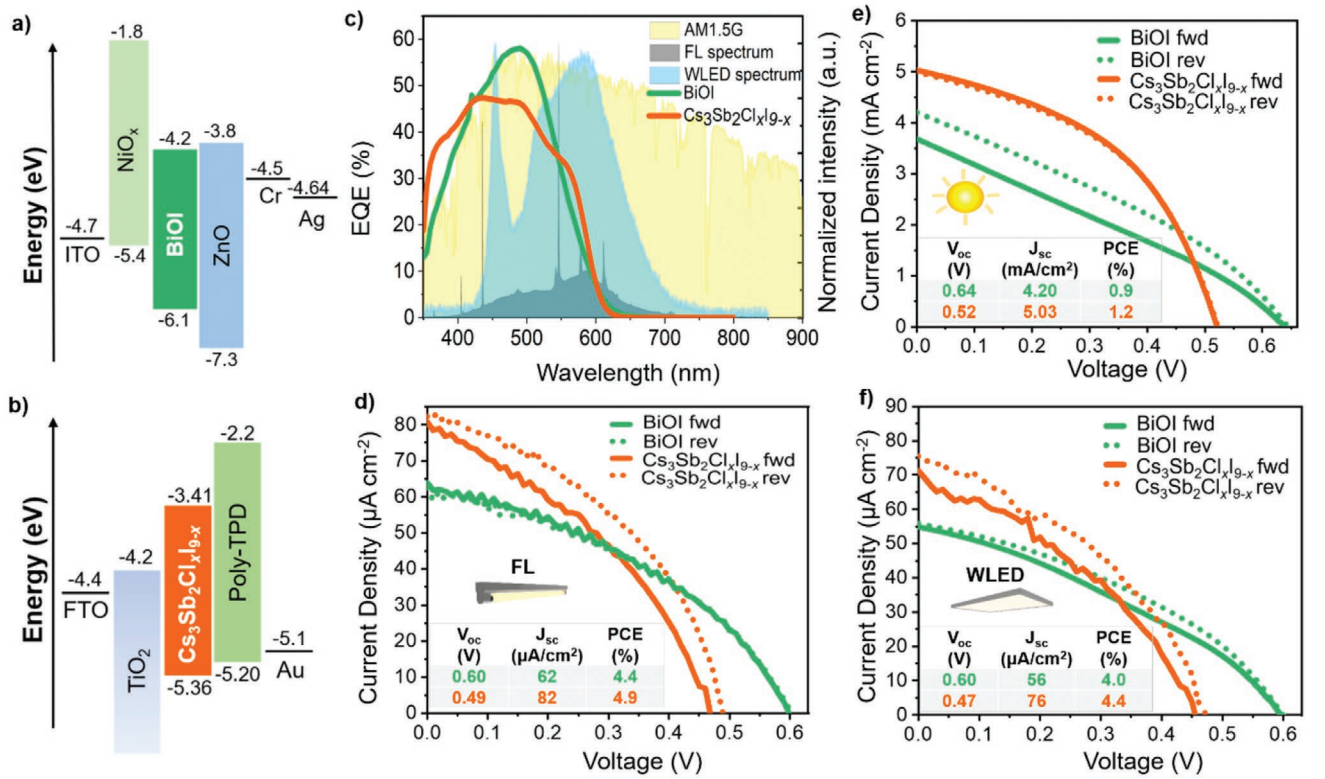

Figure 2. Band structure of the a) BiOI device stack and b) $Cs_3Sb_2Cl_xI_{9-x}$ device stack (energy values are referenced to the vacuum level). Device stacks shown in Figure S2, Supporting Information. c) EQE of BiOI and $Cs_3Sb_2Cl_xI_{9-x}$ devices, along with the FL, AM1.5G and spectra. Current density versus voltage curves of BiOI and $Cs_3Sb_2Cl_xI_{9-x}$ devices under d) FL (1000 lux), e) AM 1.5G, and f) WLED (1000 lux) illumination.

reported in the literature, possible mechanisms include: 1) oxygen passivation of layers or interfaces in the device stacks, or 2) improvement in the work function of charge transport layers, leading to improved band alignment.[60–62] While further work is needed to elucidate the exact mechanism, these results show that the materials exhibit promising stability for commercial applications, as well as very promising performance for powering IoT devices.

Table 1. Photovoltaic performance parameters of BiOI and $Cs_3Sb_2Cl_xI_{9-x}$ devices under different light sources.

			V_{oc} [V]	J_{sc} [μA cm^{-2}]	FF [%]	PCE [%]
BiOI	AM 1.5G	Forward	0.64	3680	28	0.7
		Reverse	0.64	4200	33	0.9
	WLED	Forward	0.60	55	33	3.4
		Reverse	0.60	56	38	4.0
	FL	Forward	0.60	64	35	4.3
		Reverse	0.60	62	40	4.4
$Cs_3Sb_2Cl_xI_{9-x}$	AM 1.5G	Forward	0.52	5030	48	1.2
		Reverse	0.52	5000	48	1.2
	WLED	Forward	0.45	71	37	3.7
		Reverse	0.47	76	40	4.4
	FL	Forward	0.47	81	37	4.1
		Reverse	0.49	82	42	4.9

2.2. BiOI and $Cs_3Sb_2Cl_xI_{9-x}$ Indoor Photovoltaics for Powering Thin-Film Transistor Electronics

In order to assess their significance for IoT applications, we tested the ability of mm-scale BiOI and $Cs_3Sb_2Cl_xI_{9-x}$ devices to power printed thin-film transistor (TFT) circuits. Circuits based on solution-processed TFT technologies (e.g., featuring organic semiconductors,[63,64] amorphous metal-oxide semiconductors,[65,66] and semiconducting carbon-nanotube networks[67,68]) are being intensively investigated with the aim of realizing flexible, easy-to-fabricate, and low-cost electronics for smart-sensor systems, wearable electronics, and the IoT ecosystem.[69–71] In particular, as a proof-of-concept, we investigated the ability of BiOI and $Cs_3Sb_2Cl_xI_{9-x}$ devices to power inverters (see experimental arrangement in **Figure 3**a) made with printed carbon nanotube (CNT) TFTs.[68] An inverter (also known as NOT gate) is an essential component of digital circuits, where it carries out the logic inversion of the digital signal applied at its input (i.e., it provides a "low" output for a "high" input and vice versa).

The measured voltage transfer characteristics (VTCs) of one of our inverters powered by a BiOI or a $Cs_3Sb_2Cl_xI_{9-x}$ device under FL lighting (500–1000 lux) are shown in Figure 3b,c. All measured VTCs (for all illumination levels) exhibited the expected near-step-like transition from "high" to "low" as the input signal is swept from "low" to "high." This indicates that the power supplied by the PIM devices under typical indoor illumination levels is sufficient to operate the printed TFT inverters. In fact, the power dissipated by the inverters is entirely

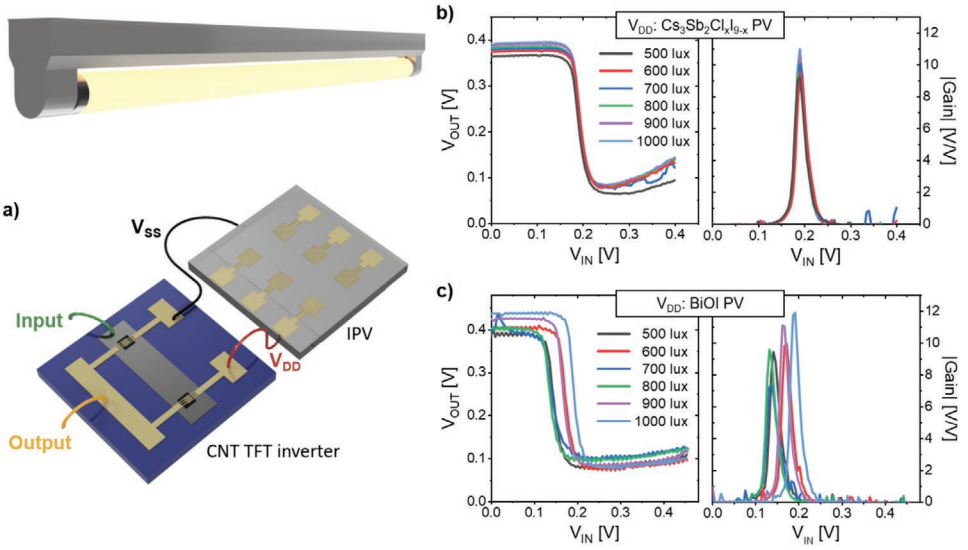

Figure 3. a) Schematic of a printed TFT inverter connected to an IPV (the terminals labelled V_{SS} and V_{DD} correspond to the power supply terminals of the inverter) operated under FL lighting. Voltage transfer characteristics and voltage gain of the inverter powered by b) $Cs_3Sb_2Cl_xI_{9-x}$ and c) BiOI devices under FL illumination (with illuminance of 500–1000 lux).

supplied by the PIM devices, from which the TFT channel current is drawn. In particular, voltage gain values (quantifying the steepness of the VTCs) greater than 7 V V^{-1} (see Figure 3b,c) are obtained at all illumination levels, denoting adequate inverter performance for robust digital signal processing. Moreover, the VTCs exhibit only minor shifts as the illumination level is varied, which can be traced to the weak dependence of the V_{oc} on light intensity (see **Figure 4**). Importantly, this implies that our IPV devices could provide sufficient power for printed TFT electronics while such electronics is moved about in an indoor environment, which opens up attractive prospects for autonomous wearable electronics.

These results demonstrate for the first time the capability of PIM IPVs to power printed TFT circuits. Crucially, we achieved this with a direct connection of one of the BiOI or $Cs_3Sb_2Cl_xI_{9-x}$ devices to a TFT circuit—i.e., without connecting several such devices in series in order to boost the overall voltage supplied, and without connecting them in parallel in order to provide sufficient current. This aspect relates to the capability of BiOI and $Cs_3Sb_2Cl_xI_{9-x}$ devices to provide a V_{oc} in the range that keeps the power dissipation of the printed TFT electronics to a minimum (i.e., devices with a larger V_{oc} would need to provide larger power for the same circuits to be able to function). It is also noteworthy that we achieved this by using BiOI and $Cs_3Sb_2Cl_xI_{9-x}$ devices with a particularly small area (7.25 mm^2), which is highly attractive for the realization of compact wearable electronic devices and smart-sensor nodes with minimal footprint (e.g., "smart dust"). In particular, the inverters employed in this proof-of-concept demonstration require a maximum current of 600 pA each to operate. Therefore, our IPV devices could supply sufficient power (while operating near V_{oc}) for electronics of complexity equivalent to ≈7000 transistors (e.g., 25 8-bit full-adders). This is a level of complexity sufficient to address real-world applications. Consequently, our proof-of-concept demonstration provides highly promising indications of the viability of the technological convergence between lead-free perovskite-inspired IPV and printed TFT electronics towards the realization of autonomous devices for emerging application areas.

2.3. Loss Analyses of BiOI and $Cs_3Sb_2Cl_xI_{9-x}$ Photovoltaics

A systematic investigation of the photoconversion mechanism of BiOI and $Cs_3Sb_2Cl_xI_{9-x}$ under low-light conditions was conducted in order to understand the main limiting factors that need to be overcome for future efficiency improvements to become possible. We characterized the optical power dependence of the open-circuit voltage (V_{oc}), fill factor (FF), and short-circuit current density (J_{sc}) over a power range of 10–200 μW cm^{-2}, which is relevant to indoor light sources. Varying the incident power density changes the quasi-Fermi level splitting, and studying how this affects the photovoltaic parameters gives insights into the dominant recombination type (trap-assisted recombination or band-to-band recombination). In these measurements, a monochromatic light source (λ = 525 nm) of varying intensity was used to ensure uniform illumination throughout the active layer. As shown in Figure 4a, the V_{oc} of BiOI devices gave a slope of ≈kT/q, while a slope of $2kT/q$ was obtained from $Cs_3Sb_2Cl_xI_{9-x}$ devices (where T is the device temperature, k the Boltzmann's constant, and q the elementary charge). A slope equal to $2kT/q$ (≈0.050 V at room temperature) in the V_{oc} versus light intensity plot has been associated with defect-assisted (Shockley-Read-Hall, SRH) recombination involving mid-gap states in the absorber.[72–75] Therefore, the observed light-intensity dependence of the V_{oc} of $Cs_3Sb_2Cl_xI_{9-x}$ devices suggests that they are predominantly limited by nonradiative recombination. This is consistent with the low photoluminescence quantum efficiency (PLQE) of $Cs_3Sb_2Cl_xI_{9-x}$, which we measured to be ≈0.1%, demonstrating recombination to be dominated by non-radiative processes. This may be related to the smaller grain size of $Cs_3Sb_2Cl_xI_{9-x}$

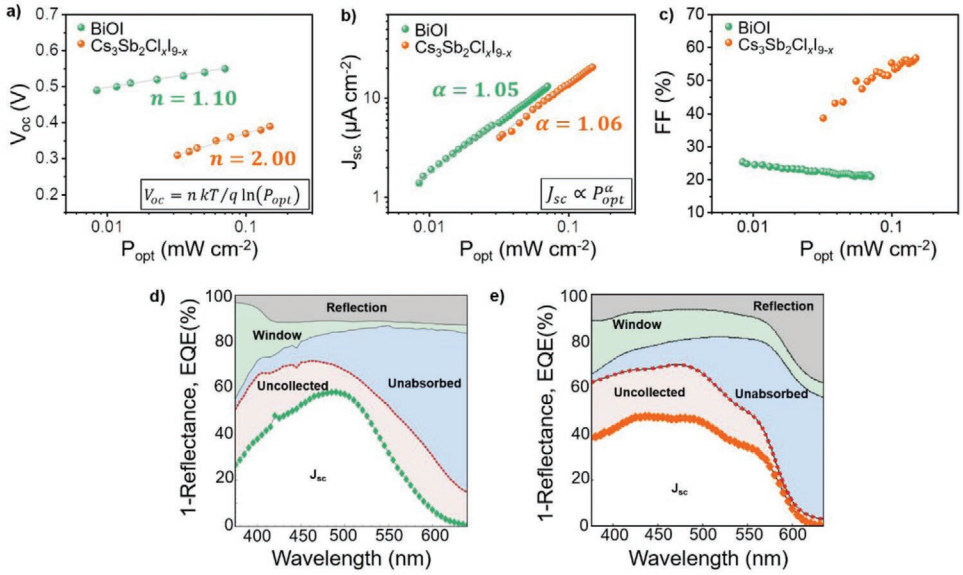

Figure 4. Optical power dependence of a) V_{oc}, b) J_{sc}, and c) FF of BiOI and $Cs_3Sb_2Cl_xI_{9-x}$ devices under monochromatic illumination at $\lambda = 525$ nm over a power range of the same order and lower than that of indoor light sources at 1000 lux. Optical loss analyses of d) BiOI and e) $Cs_3Sb_2Cl_xI_{9-x}$ devices.

films, and possibly the presence of deep recombination centers. The discontinuous morphology of the $Cs_3Sb_2Cl_xI_{9-x}$ layers could also contribute to nonradiative recombination in devices (Figure 1c). With regard to BiOI, while a slope equal of kT/q in the V_{oc} versus light intensity plot has been customarily attributed to band-to-band recombination, this is not consistent with our previous results, in which we showed the fluence-independence of the decay in photoluminescence (from time-correlated single photon counting measurements) and ground-state bleach (from transient absorption spectroscopy measurements).[45,58,74] Furthermore, we measured the PLQE of BiOI, which we found to be <0.1%. These results suggest that recombination in BiOI is dominated by nonradiative processes. In fact, a slope of kT/q in the V_{oc} versus light intensity plot of BiOI devices could also originate from SRH recombination through shallow or mid-gap defect states in the presence of a high majority carrier concentration.[74,75] This could arise in the BiOI devices due to the space-charge region that could form next to the NiO_x hole transport layer (illustrated in Figure S6, Supporting Information). We previously found, from systematic X-ray and ultraviolet photoemission spectroscopy measurements, that BiOI exhibits downwards band-bending next to the interface with NiO_x, owing to the lower work function of NiO_x compared to BiOI.[45] Such downwards band-bending could cause an accumulation of electrons next to the NiO_x/BiOI interface under illumination, leading to the formation of a space-charge region (refer to Figure S6, Supporting Information).

The trend in FF with light intensity may provide further insights into the recombination mechanism. For $Cs_3Sb_2Cl_xI_{9-x}$, the FF increases with increasing light intensity (Figure 4c). This may be due to SRH recombination. The population of mobile carriers increases with increasing light intensity, while the density of traps remains the same. The FF trend for $Cs_3Sb_2Cl_xI_{9-x}$ in Figure 4c therefore seems to be consistent with its measured V_{oc} dependence on light intensity. Another possibility, however, is that the FF increases with light intensity due to a shunting effect, which is also suggested by the imperfections in the $Cs_3Sb_2Cl_xI_9$ layer we observed via SEM (see Figure 1c). On the other hand, BiOI exhibits a reduction in FF with increasing light intensity. This agrees with our previous intensity-dependent FF measurements made at higher light intensities (20–100 mW cm^{-2}) and is consistent with the effects of a space-charge region in BiOI next to the interface with NiO_x.[45] At lower light intensities, there is a smaller population of photogenerated carriers, hence a smaller space-charge region forms, and a larger fraction of carriers can be extracted. This indicates that BiOI devices made with the current device structure are more suitable for lower light-intensity applications.

Finally, the trends in J_{sc} with light intensity give insight into the dominant recombination mechanisms at short-circuit conditions. Both $Cs_3Sb_2Cl_xI_{9-x}$ and BiOI devices exhibit a linear trend (Figure 4b), which is consistent with our previous observations at higher light intensities (20–100 mW cm^{-2}), and is suggestive of defect-assisted recombination through mid-gap states.[39,56,76]

To corroborate our analysis of the intensity-dependent performance measurements, we performed optical loss analyses. For both devices, the largest loss in current is due to unabsorbed photons. This is slightly larger for BiOI (31–38%) than for $Cs_3Sb_2Cl_xI_{9-x}$ (29% under 1 sun; ≈34% under indoor lighting; **Table 2**), which is in part due to BiOI having a lower absorption coefficient than $Cs_3Sb_2Cl_xI_{9-x}$ (Figure 1d). Improved light management to reduce optical losses (e.g., nanophotonic structures at the back electrode) would improve performance. Beyond unabsorbed photons, the next largest loss in current is due to uncollected carriers. This is larger in BiOI, where this loss process accounts for 20% of the current under all illumination conditions (Table 2). This is consistent with the intensity-dependent analyses above and also the optical loss analyses in our previous work, in which carriers were found to be lost due to sub-optimal band alignment in the device stack.[45] In $Cs_3Sb_2Cl_xI_{9-x}$, uncollected carriers account for 16% of the

Table 2. Losses in current density from the different layers in BiOI and $Cs_3Sb_2Cl_xI_{9-x}$ devices.

Sample	BiOI			$Cs_3Sb_2Cl_xI_{9-x}$		
Illumination	FL	WLED	AM 1.5G	FL	WLED	AM 1.5G
Reflection loss (μA cm^{-2})	14.6	14.6	1740	19.5	19.5	2067
Loss from window layers (μA cm^{-2})	3.2	2.6	689.1	11.6	11.3	1495.9
Loss from unabsorbed photons (μA cm^{-2})	45.8	46.8	4773.9	43.0	44.0	4252.1
Uncollected carriers (μA cm^{-2})	24.8	24.2	2998.4	17.1	16.6	2371.4
J_{sc} (μA cm^{-2})	35.8	35.3	5091.9	35.6	34.8	4736.9

current under indoor lighting and 19% under 1 sun illumination (Table 2), which may arise from nonradiative recombination.

All things considered, the loss analyses show that one of the ways to improve the performance of $Cs_3Sb_2Cl_xI_{9-x}$ IPVs is to optimize the morphology in order to achieve a continuous film and larger grains. For BiOI, on the other hand, IPV performance could be improved by developing higher work function hole transport layers that prevent downwards band bending while maintaining dense, a/b-axis oriented platelets. The next question is what efficiencies these materials could achieve if all parasitic optical losses and limitations due to sub-optimal morphology or band positions could be eliminated. This is discussed in the next section.

2.4. Future IPV Potential of Lead-Free Perovskite-Inspired Materials

Similar to BiOI and $Cs_3Sb_2Cl_xI_{9-x}$, there is a wide range of PIMs that have demonstrated modest photovoltaic performances under 1-sun conditions (typical PCEs of ≈1–2%) but have bandgaps that are more suited for indoor light sources.[44,46] To provide direction for the future exploration of the broader family of PIMs for indoor light harvesting, we calculated the theoretical efficiency limits (see Note S1, Supporting Information, for details on methodology) for BiOI and $Cs_3Sb_2Cl_xI_{9-x}$, as well as a range of commonly investigated PIMs: rudorffites (Ag-Bi-I), vacancy-ordered double perovskites (Cs_2TiBr_6), binary halides (BiI_3, InI), and defect-ordered perovskites ($A_3B_2X_9$ absorbers). In this section, we first discuss the future potential of $Cs_3Sb_2Cl_xI_{9-x}$ and BiOI, before identifying other classes of PIMs that hold significant potential for IPV, which are worth future investigation.

The efficiency limits were calculated for FL and WLED sources with power density values of 3.4 and 3.2 W m^{-2} respectively (which correspond to the 1000 lux illuminance of the sources used in this work). A theoretical maximum efficiency of ≈62% can be reached under both FL and WLED lighting with absorbers possessing a bandgap of 1.9 eV (**Figure 5**) based on the detailed balance approach taken by Shockley and Queisser.[77] While the radiative limit (RL) gives an indication of the magnitude of the IPV efficiency that can be reached, it does not account for materials properties such as the absorption coefficient, and degree of non-radiative recombination at open circuit voltage conditions, which depend on the direct/indirect nature of the bandgap. A more realistic efficiency limit can be calculated by taking into account the absorptance, thickness of the absorber, and nature of the bandgap (direct vs indirect), along the lines pursued by Zunger et al. in their definition of the spectroscopically limited maximum efficiency (SLME).[78] It is noteworthy that, while the SLME limit has been applied to calculate the 1-sun optically limited efficiency of materials, to the best of our knowledge, a similar concept has not been applied to assess the potential of materials for IPV applications. Therefore, here we introduce the IPV-equivalent of the SLME, which accounts for the spectra of the indoor light sources, and we refer to it as the indoor SLME (i-SLME in short form; see Note S1, Supporting Information, for details). While SLME values are typically calculated using the absorptance derived from computed absorption coefficient values,[78] in this work we calculated i-SLME values based on the experimentally measured absorption coefficients reported in the literature, which would be more reflective of the maximum IPV efficiencies that could be ultimately reached. For all absorbers, a thickness of 500 nm was taken in the i-SLME calculations.

Although BiOI and $Cs_3Sb_2Cl_xI_{9-x}$ have very similar RL efficiency values (Figure 5), BiOI has a shallower absorption onset and a lower absorption coefficient than $Cs_3Sb_2Cl_xI_{9-x}$ (≈10^4 vs ≈10^5 cm^{-1}, respectively; Figure 1d). As a result, in the i-SLME limit, the J_{sc} and V_{OC} of BiOI are lower (Figure 5; Tables S2 and S3 and Figure S7, Supporting Information). Even if we take the extreme case where the fraction of radiative recombination (f_r) is 1 (i.e., we have a direct bandgap), the maximum efficiency would be only 44% under FL and WLED

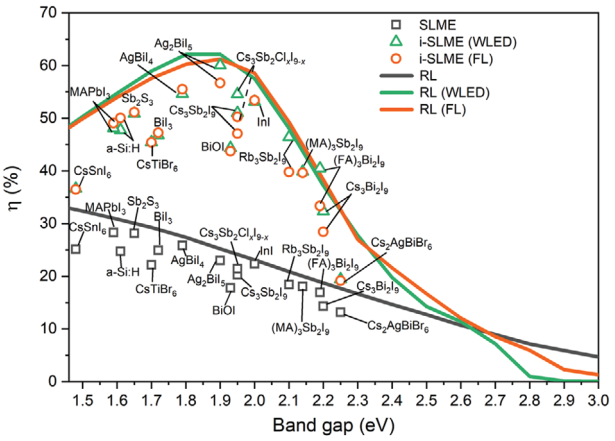

Figure 5. Radiative limit and Spectroscopically Limited Maximum Efficiency (SLME) of the photovoltaic efficiencies of lead-free perovskite-inspired materials under AM 1.5G and indoor lighting conditions. The corresponding values for a-Si:H and $MAPbI_3$ are also included as references.

illumination. Films thicker than 500 nm would increase the proportion of absorbed photons but could lead to increased series resistance. Thus, although BiOI has achieved a similar PCE under indoor lighting as $Cs_3Sb_2Cl_xI_{9-x}$, we would expect that $Cs_3Sb_2Cl_xI_{9-x}$ could ultimately achieve higher IPV performance with optimized morphology and device structure (see Section 2.3). Nevertheless, BiOI has the important advantages of being stable in air without encapsulation, and processable using a scalable t-CVD method.[45] These advantages will be important for commercial applications, and future development of BiOI for IPV is warranted.

Our analysis also illustrates the importance of being able to control the polymorphism in the $Cs_3Sb_2I_9$ system. Figure 5 shows that the 0D structure has i-SLMEs that are approximately 5% lower than the 2D structure. This is primarily due to the lower V_{OC} of the 0D compound. The 0D polymorph has an indirect bandgap, whereas the 2D structure has a bandgap that is nearly direct.[47,50,56] This results in the 0D compound having a smaller f_r value, which lead to a lower calculated V_{OC} value (refer to Tables S1–S3, Supporting Information). The layered $Cs_3Sb_2Cl_xI_{9-x}$ compound is therefore a promising material for further investigations for IPV and has some of the highest predicted i-SLMEs (50–54%; see Figure 5).

In order to benchmark these findings, it is useful to compare them against a-Si:H, which is the workhorse compound for IPV. While the i-SLMEs of a-Si:H are at 47–50% (Figure 5; Tables S2 and S3, Supporting Information), a-Si:H has an IPV efficiency that has long saturated to values in the range of 4.4–9.2%.[15,20–22] BiOI and $Cs_3Sb_2Cl_xI_{9-x}$ provide IPV efficiencies that are already in the same range as a-Si:H (see Section 2.1). Considering that this is the first report on BiOI and $Cs_3Sb_2Cl_xI_{9-x}$ for indoor light harvesting, and that we have already identified strategies that could enable future increases in their IPV efficiencies (see Section 2.3), our i-SLME calculations confirm the potential of BiOI and $Cs_3Sb_2Cl_xI_{9-x}$ to surpass the IPV performance of a-Si:H.

Beyond $Cs_3Sb_2Cl_xI_{9-x}$ and BiOI, our analysis in Figure 5 shows that there is a wide range of other PIMs that are highly promising for IPV and have significant potential to exceed the performance of a-Si:H IPV. These include the $Ag_aBi_bI_x$ ($x = a + 3b$) rudorffites (e.g., $AgBiI_4$ and Ag_2BiI_5) and Sb_2S_3, which have i-SLMEs in the region of 50–60%. Both classes of materials have shown very promising efficiencies to date under 1-sun illumination.[79–81] We note that Sb_2S_3 is limited by the formation of self-trapped excitons, which leads to unavoidable losses at room temperature and limits the open-circuit voltage. Nevertheless, Sb_2S_3 solar cells have achieved 6% PCE under 1-sun illumination, with an estimated 1-sun efficiency limit of 16%.[82,83] Given their close match with the indoor light spectrum, Sb_2S_3 devices are very likely to achieve IPV efficiencies well above 10%. Therefore, coupled with its stable performance in ambient air, Sb_2S_3 is worth future investigations for IPV.[83]

IPV efficiencies higher than a-Si:H could also be expected from $Rb_3Sb_2I_9$, which, just like BiOI and $Cs_3Sb_2Cl_xI_{9-x}$, is a layered compound with high mobility planes that allow photogenerated charges to be efficiently extracted.[32,50] $MA_3Sb_2I_9$ is another potential material. Although the i-SLMEs of the 0D compound are low, recent work has shown that the 2D phase can be stabilized, leading to a near-direct bandgap (which allows higher absorption coefficients) and a lower bandgap value of 2.1 eV (which is closer to the optimum for IPV).[84]

InI is another material with high i-SLMEs of 53%. However, InI devices have demonstrated relatively poor 1-sun photovoltaic efficiencies of ≈0.4%.[85] Furthermore, InI has been reported to oxidize easily due to the relative instability of In^+ compared to In^{3+}, and this will likely limit its potential applications in both outdoor and indoor photovoltaics. This limitation is not present in the materials discussed earlier based on Bi^{3+} and Sb^{3+}, which are in their most stable oxidation states.[83,86,87]

3. Conclusion

In this work, we explored, for the first time, the capability and potential of lead-free perovskite-inspired absorbers for indoor photovoltaics. We examined in detail two exemplar PIMs, BiOI and $Cs_3Sb_2Cl_xI_{9-x}$. These materials are photostable and have bandgaps close to 1.9 eV, which is too wide for efficiently harvesting solar radiation in single-junction devices, but is optimal for indoor light harvesting. Whereas the PCEs were only approximately 1% under 1-sun illumination, the same devices reached PCEs of 4–5% under FL and WLED lighting, with peak values of 4.4% for BiOI devices and 4.9% for $Cs_3Sb_2Cl_xI_{9-x}$ devices under FL lighting. This is already comparable to the IPV performance of industry-standard a-Si:H. We showed that our mm-scale PIM IPVs had V_{OC} values that were sufficient for powering printed thin-film-transistor electronics, demonstrating the potential of such IPVs to power indoor IoT devices. Critically, our loss analyses showed that our PIM IPVs can still achieve further increases in efficiency. Moreover, the efficiency limits calculated based on their absorption coefficients show that these materials have significant potential for exceeding the performance of industry-standard a-Si:H IPV. More broadly, we calculated the spectroscopically-limited maximum efficiency of the most common PIMs explored in the wider field that have bandgaps between 1.45 and 2.3 eV. From this analysis, we identified that the silver-bismuth-iodide rudorffites and Sb_2S_3, and possibly also $Rb_3Sb_2I_9$ and $MA_3Sb_2I_9$ (particularly the 2D polymorph), are also very promising for IPV applications. Overall, this work encourages researchers to regard IPV as a key target area in the future exploration of perovskite-inspired materials. In particular, the attractive optoelectronic properties and low-toxicity profile of many wide-bandgap PIMs provide a formidable opportunity for the development of nontoxic, stable and efficient IPV that can sustainably power the rapidly growing IoT device ecosystem.

4. Experimental Section

Chemicals were used as purchased without additional purification. CsI (99.999%, Alfa Aesar), SbI_3 (99.999%, Sigma-Aldrich), $SbCl_3$ (99.999%, Alfa Aesar), *N*,*N*-dimethylfomamide (DMF) (analytical grade, Beijing Chemical Reagent Co.), dimethylsulfoxide (DMSO) (analytical grade, Beijing Chemical Reagent Co.), titanium(IV) isopropoxide (Sigma-Aldrich), titania paste (18NR-T, Greatcell Solar), poly[N,N′-bis(4-butylphenyl)-N,N′-bisphenylbenzidine] (poly-TPD) (Lumtec), toluene (super-dry, Beijing Chemical Reagent Co.), chlorobenzene (CB) (>99%, J&K). BiI_3 (99.998% Sigma Aldrich), nickel nitrate hexahydrate (Sigma Aldrich), ethylene glycol (Sigma Aldrich), ethylenediamine (Sigma Aldrich), diethylzinc (Sigma Aldrich).

Preparation of $Cs_3Sb_2Cl_xI_{9-x}$ Thin Films: The deposition of $Cs_3Sb_2Cl_xI_{9-x}$ thin films was carried out through a previously reported procedure.[56] CsI, SbI_3, and $SbCl_3$ powders with molar ratio of 3:2:1 were dissolved in a solvent mixture (DMSO:DMF, 3:1 volume ratio) to prepare a 0.3 M precursor solution. The solution was continuously stirred overnight at 70 °C and then filtered using a polytetrafluoroethylene (PTFE) filter with 0.22 µm pore size before use. Subsequently, 40 µL of the resulting solution were spin-coated at 4000 rpm for 30 s and 150 µL of toluene (serving as antisolvent) were dispensed onto the rotating substrate during the last 10 s of the spin-coating cycle. Finally, solvent vapor annealing was carried out, during which the samples were placed inside a Petri dish containing 5 µL of DMSO and annealed at 135 °C for 30 min.

Fabrication of $Cs_3Sb_2Cl_xI_{9-x}$ Devices: Patterned glass/fluorine-doped tin-oxide (FTO) substrates from Ying Kou You Xuan Trade Co. Ltd (FTO sheet resistance of 7–9 Ω sq^{-1}) were successively sonicated in baths containing detergent in deionized water, acetone, and ethanol (10 min each). UV-ozone treatment was further implemented for 30 min after drying the substrates under N_2 gas flow. A compact TiO_2 (c-TiO_2) layer was prepared by spin-coating a mixed solution of 5.06 mL of isopropyl alcohol, 380 µL of titanium(IV) isopropoxide, and 35 µL of dilute HCl (as detailed in ref. [88]) at 4000 rpm for 30 s and sintered at 450 °C for 40 min in air. In order to obtain a thin mesoporous TiO_2 (m-TiO_2) layer, titania paste was spin-coated at 7000 rpm for 60 s and then sintered at 450 °C for 40 min. Subsequently, the procedure detailed in the Preparation of $Cs_3Sb_2Cl_xI_{9-x}$ Thin Films subsection above was performed to deposit the perovskite layer. A 10 mg mL^{-1} solution of poly-TPD in chlorobenzene was spin-coated at 4000 rpm for 30 s. Finally, the top electrodes (40 nm thick Au) were deposited by thermal evaporation, defining a device active area of 7.25 mm^2.

Preparation of BiOI Thin films: t-CVD was used to deposit BiOI following a previously reported method.[45] A two-zone furnace with a quartz tube was used for the deposition. Zone 1 was pre-heated to 360 °C while zone 2 was set to 350 °C. For each growth run, four substrates were attached to a microscope glass slide with silver paste (Electrolube) and loaded into the quartz tube. A ceramic crucible loaded with 500 mg of BiI_3 powder was placed close to the heating roads in zone 1. The substrates were placed at least 8 cm away from the crucible containing the BiI_3 precursor. A gas mixture of Ar and O_2 (19 mL min^{-1} Ar, 4.5 mL min^{-1} O_2) was used as the carrier gas and oxidant.

Fabrication of BiOI Devices: Patterned glass/indium-tin-oxide (ITO) substrates from South China Science & Technology Co. Ltd (ITO sheet resistance of <30 Ω sq^{-1}) were sequentially ultrasonically cleaned in acetone and isopropyl alcohol for 15 min. This was followed by O_2 plasma treatment (Zepto, Diener) at 100 W for 10 min. The hole transport layer, NiO_x, was deposited via a sol-gel spin coating process described in a previous report.[58] A drop of Ni sol (1 mol L^{-1} nickel nitrate hexahydrate in ethylene glycol with 1 mol L^{-1} ethylenedinamine) was filtered through a 0.22 µm PTFE filter and spread onto the substrates. The substrates were spun for 45 s at 5000 rpm and annealed on a hotplate (Stuart UC152D) at 125 °C for 40 min followed by a longer anneal at 300 °C for 70 min. The films were quenched on an Al foil after unloading from the hotplate. The NiO_x-coated substrates were spun with Ni sol for a second time to form a double layer of NiO_x (≈30 nm thickness) and pinhole-free coverage of the substrate.

Following BiOI growth using the method detailed above, the electron transport layer, ZnO was deposited using an atmospheric pressure spatial atomic layer deposition system (in the CVD growth regime). Diethylzinc and O_2 were the precursors used. The top electrode, 20 nm Cr and 100 nm Ag was thermally evaporated onto the device stack through the use of a shadow mask. The overlap between the Cr/Ag top electrode and the bottom ITO electrode defined the device area, which amounted to 7.25 mm^2.

Materials Characterization: XRD: 1D θ–2θ linescans of rotating BiOI samples were measured in air with a Bruker D8 diffractometer with Cu K_α radiation (λ = 1.5406 Å), which had a tube current 40 mA and a generator voltage of 40 kV. XRD patterns of $Cs_3Sb_2Cl_xI_{9-x}$ films were measured in air with a Panalytical Empyrean X-ray diffractometer (λ = 1.5406 Å, tube current = 40 mA, generator voltage = 40 kV).

Materials Characterization: SEM: The top down electron microscopy image for BiOI was taken using FEI Magellan (XHR 400L) scanning electron microscope using an accelerating voltage of 10 kV (pressure of 10^{-5} mbar). The top down electron microscopy image of $Cs_3Sb_2Cl_xI_{9-x}$ films was acquired using a Zeiss GeminiSEM 500 scanning electron microscope, at a pressure of 2×10^{-5} mbar and with an accelerating voltage of 10 kV.

Materials Characterization:UV–Vis Spectrophotometry: The absorption coefficient of BiOI, along with the transmittance and reflectance of the BiOI device stack for optical loss analyses were obtained from ref. [45]. For $Cs_3Sb_2Cl_xI_{9-x}$, the transmittance (T) and reflectance (R) of the thin film on glass were measured within an integrating sphere using a Shimadzu UV-3600 Plus UV-VIS-NIR spectrophotometer. The absorption coefficient (α) was calculated from $\alpha = -\ln[T/(1-R)]/t$, in which t is the film thickness (measured by Dektak profilometry), and R and T are given as fractions. The absorptance obtained from these measurements was used in the optical loss analyses of $Cs_3Sb_2Cl_xI_{9-x}$ devices. In these optical loss analyses, the transmittance of the window layers was measured with a PerkinElmer LAMBDA 750 UV/Vis/NIR spectrophotometer, while reflectance measurements were carried out with a PerkinElmer Lambda 950 UV–Vis–NIR spectrophotometer. The equations used for the optical analysis are detailed in Section S5 of the Supporting Information of our previous work.[45] Briefly, the reflectance spectra of the complete device (measured from the glass side, which is the direction of illumination under operation), as well as the absorptance spectra of the window layers (glass, ITO and NiO_x for BiOI devices; glass, FTO and TiO_2 for $Cs_3Sb_2Cl_xI_{9-x}$) were multiplied with the incident light spectrum, integrated and multiplied with a factor of q/10 to calculate the current densities lost due to reflection and parasitic absorption. The absorption coefficients of BiOI and $Cs_3Sb_2Cl_xI_{9-x}$ and the EQEs of the respective devices were used to determine the current density lost due to unabsorbed photons, as well as photons that are absorbed but not collected.

Materials Characterization - Photoluminescence Quantum Efficiency (PLQE): Measurements were performed in accordance with the report by de Mello et al.[89] Excitation was performed with a continuous wave laser with a wavelength of 405 nm. A power density of 700 mW cm^{-2} was used. A Maya fixed grating spectrometer was used (300/ BLZ 500 nm), with a slit width of 200 µm, exposure time of 0.2 s and with 100 accumulations. The background was subtracted.

Optoelectronic Characterization: External quantum efficiency (EQE) measurements were carried out in air using a source meter (Keithley 6420). The customized EQE setup containing a monochromated light source (Zolix Omni-λ2005i) was calibrated with a power meter assembly (Thorlabs PM200 and Thorlabs S120VC).

Variable-power measurements of short-circuit current, open-circuit voltage, and fill-factor were conducted with a high-power 525 nm LED source (Thorlabs SOLIS-525C), optical filters (Zolix), and a semiconductor parameter analyzer (Tektronix, 4200A-SCS).

Photovoltaic Measurements: The current density–voltage (J–V) characteristics of photovoltaic devices under simulated solar illumination were acquired using a solar simulator calibrated to give AM 1.5G (100 mW cm^{-2}) radiation, equipped with a standard Xenon lamp (Newport) together with a Keithley 2400 source meter.

The J–V characteristics of photovoltaic devices under indoor illumination were measured using a Keithley 4200A-SCS semiconductor parameter analyzer (Tektronix) together with a custom-made optical setup. The two light sources employed were a fluorescent lamp (HLSF218 2 × 18W) and a white LED panel (Biard BLPAN303065). The lamps were adjusted to the appropriate height in order to achieve an illuminance of 1000 lux on the photovoltaic device surface. The illuminance was calibrated with an auto-ranging light meter (ATP DT-1309). The corresponding irradiance (W cm^{-2}) on the photovoltaic device surface was determined by combining an optical power measurement (conducted with a Thorlabs PM200 and Thorlabs S120VC) and an optical spectrum measurement (using a Firefly 4000 LASERTECH). This allowed us to determine that the FL and WLED

sources at 1000 lux had an irradiance of 340 and 320 μW cm^{-2}, respectively. The accuracy of the light meter and power meter is the primary determinant of the uncertainty in the measured PCE values, which amounts to approximately ±6–7%, as can be determined from a straightforward uncertainty analysis based on the device testing conditions and the specifications of the power and light meters. Consequently, the PCE values are reported herein with 1 decimal place.

Supporting Information

Supporting Information is available from the Wiley Online Library or from the author. The raw data can be found from https://doi.org/10.14469/hpc/7521.

Acknowledgements

T.N.H. acknowledges funding from the EPSRC Centre for Doctoral Training in Graphene Technology (No. EP/L016097/1) and the Aziz Foundation. L.P. acknowledges support from the National Natural Science Foundation of China (61950410619). R.A.J. acknowledges support from a DTP studentship funded by EPSRC (No.: EP/N509620/1). R.A.J. and J.L.M.-D. thank Bill Welland for financial support, as well as the Winton Programme for the Physics of Sustainability. J.L.M.-D. acknowledges support from the Royal Academy of Engineering grant CIET1819\24. R.L.Z.H. acknowledges support from the Royal Academy of Engineering under the Research Fellowship programme (RF\201718\1701), the Isaac Newton Trust (Minute 19.07(d)) and Downing College Cambridge through the Kim and Juliana Silverman Research Fellowship. V.P. acknowledges financial support from the National Natural Science Foundation of China (61950410759, 61805166), the Jiangsu Province Natural Science Foundation (BK20170345), the Collaborative Innovation Center of Suzhou Nano Science & Technology, the Priority Academic Program Development of Jiangsu Higher Education Institutions (PAPD), the 111 Project, and the Joint International Research Laboratory of Carbon-Based Functional Materials and Devices.

Conflict of Interest

The authors declare no conflict of interest.

Author Contributions

Y.P., T.N.H., and J.M. contributed equally to this work. V.P. conceived the project. V.P. and R.L.Z.H. led this project. Y.P. and J.M. fabricated and characterized the $Cs_3Sb_2I_{9-x}Cl_x$ thin films (via SEM and XRD), as well as the EQE and photovoltaic performance of both $Cs_3Sb_2I_{9-x}Cl_x$ and BiOI devices (under indoor, AM 1.5G, and variable-power monochromatic illumination), under the supervision of V.P. T.N.H. grew the BiOI thin films, characterized their morphology and phase-purity, and contributed to their development into devices. R.L.Z.H. performed the photostability measurements. J.M. (supervised by V.P.) and R.A.J. (supervised by R.L.Z.H.) performed the UV–visible spectrophotometry measurements. Using these optical measurements, T.N.H. performed the optical loss analyses (supervised by R.L.Z.H.) T.N.H., with the help of R.A.J, computed the Shockley-Queisser limit and spectroscopically limited maximum efficiencies, under the supervision of R.L.Z.H. L.P. characterized the TFT circuits powered by the IPV devices, under the supervision of V.P. All authors discussed the results and contributed to writing the article.

Keywords

antimony-based perovskite derivatives, bismuth oxyiodide, indoor photovoltaics, Internet of Things, perovskite-inspired absorbers

Received: August 27, 2020
Revised: October 19, 2020
Published online:

[1] E. Abad, F. Palacio, M. Nuin, A. G. de Zárate, A. Juarros, J. M. Gómez, S. Marco, *J. Food Eng.* **2009**, *93*, 394.
[2] H. Jin, T.-P. Huynh, H. Haick, *Nano Lett.* **2016**, *16*, 4194.
[3] M. Xie, K. Hisano, M. Zhu, T. Toyoshi, M. Pan, S. Okada, O. Tsutsumi, S. Kawamura, C. Bowen, *Adv. Mater. Technol.* **2019**, *4*, 1800626.
[4] J. Gao, *Machine Learning Applications for Data Center Optimization*, https://storage.googleapis.com/gweb-sustainability.appspot.com/pdf/42542.pdf (accessed: August 2020).
[5] M. Li, C. Zhao, Z. Wang, C.-C. Zhang, H. K. H. Lee, A. Pockett, J. Barbé, W. C. Tsoi, Y. Yang, M. J. Carnie, X.-Y. Gao, W.-X. Yang, J. R. Durrant, L.-S. Liao, S. M. Jain, *Adv. Energy Mater.* **2018**, *8*, 1801509.
[6] J. Dagar, S. Castro-Hermosa, G. Lucarelli, F. Cacialli, T. M. Brown, *Nano Energy* **2018**, *49*, 290.
[7] A. Keshavarzi, W. van den Hoek, *IEEE Des. Test* **2019**, *36*, 41.
[8] I. Mathews, S. N. Kantareddy, T. Buonassisi, I. M. Peters, *Joule* **2019**, *3*, 1415.
[9] P. Harrop, *Battery Elimination in Electronics and Electrical Engineering 2018-2028*, https://www.idtechex.com/en/research-report/battery-elimination-in-electronics-and-electrical-engineering-2018-2028/550 (accessed: October 2020).
[10] D. L. Dilaura, K. W. Houser, R. G. Mistrick, G. R. Steffy, *The Lighting Handbook Reference and Application*, Illuminating Engineering Society of North America, NY, USA **2011**.
[11] C. Y. Chen, Z. H. Jian, S. H. Huang, K. M. Lee, M. H. Kao, C. H. Shen, J. M. Shieh, C. L. Wang, C. W. Chang, B. Z. Lin, C. Y. Lin, T. K. Chang, Y. Chi, C. Y. Chi, W. T. Wang, Y. Tai, M. De Lu, Y. L. Tung, P. T. Chou, W. T. Wu, T. J. Chow, P. Chen, X. H. Luo, Y. L. Lee, C. C. Wu, C. M. Chen, C. Y. Yeh, M. S. Fan, J. De Peng, K. C. Ho, Y. N. Liu, H. Y. Lee, C. Y. Chen, H. W. Lin, C. Te Yen, Y. C. Huang, C. S. Tsao, Y. C. Ting, T. C. Wei, C. G. Wu, *J. Phys. Chem. Lett.* **2017**, *8*, 1824.
[12] B. Minnaert, P. Veelaert, *Energies* **2014**, *7*, 1500.
[13] C. L. Cutting, M. Bag, D. Venkataraman, *J. Mater. Chem. C* **2016**, *4*, 10367.
[14] K. Ruhle, M. Kasemann, Approaching High Efficiency Wide Range Silicon Solar Cells, *2013 IEEE 39th Photovoltaic Specialists Conference (PVSC)*, Tampa, FL, **2013**, pp. 2651–2654.
[15] M. Freunek, M. Freunek, L. M. Reindl, *IEEE J. Photovoltaics* **2013**, *3*, 59.
[16] A. S. Teran, J. Wong, W. Lim, G. Kim, Y. Lee, D. Blaauw, J. D. Phillips, *IEEE Trans. Electron Devices* **2015**, *62*, 2170.
[17] M. Freitag, J. Teuscher, Y. Saygili, X. Zhang, F. Giordano, P. Liska, J. Hua, S. M. Zakeeruddin, J. E. Moser, M. Grätzel, A. Hagfeldt, *Nat. Photonics* **2017**, *11*, 372.
[18] C.-Y. Y. Chen, W.-H. H. Lee, S.-Y. Y. Hsiao, W.-L. L. Tsai, L. Yang, H.-L. Lin, H.-J. Chou, H.-W. Lin, *J. Mater. Chem. A* **2019**, *7*, 3612.
[19] H. K. H. Lee, J. Wu, J. Barbé, S. M. Jain, S. Wood, E. M. Speller, Z. Li, F. A. Castro, J. R. Durrant, W. C. Tsoi, *J. Mater. Chem. A* **2018**, *6*, 5618.
[20] D. T. Cotfas, P. A. Cotfas, *Int. J. Photoenergy* **2019**, *2019*, 1905041.
[21] G. Apostolou, A. Reinders, M. Verwaal, *Energy Sci. Eng.* **2016**, *4*, 69.
[22] *Photovoltaic Modeling Handbook*, (M. F. Müller), John Wiley & Sons, Inc., Hoboken, NJ **2018**.

[23] F. De Rossi, T. Pontecorvo, T. M. Brown, *Appl. Energy* **2015**, *156*, 413.
[24] M. Kim, G. H. Kim, T. K. Lee, I. W. Choi, H. W. Choi, Y. Jo, Y. J. Yoon, J. W. Kim, J. Lee, D. Huh, H. Lee, S. K. Kwak, J. Y. Kim, D. S. Kim, *Joule* **2019**, *3*, 2179.
[25] X. Zheng, J. Troughton, N. Gasparini, Y. Lin, M. Wei, Y. Hou, J. Liu, K. Song, Z. Chen, C. Yang, B. Turedi, A. Y. Alsalloum, J. Pan, J. Chen, A. A. Zhumekenov, T. D. Anthopoulos, Y. Han, D. Baran, O. F. Mohammed, E. H. Sargent, O. M. Bakr, *Joule* **2019**, *3*, 1963.
[26] P. K. Nayak, S. Mahesh, H. J. Snaith, D. Cahen, *Nat. Rev. Mater.* **2019**, *4*, 269.
[27] A. K. Jena, A. Kulkarni, T. Miyasaka, *Chem. Rev.* **2019**, *119*, 3036.
[28] M. D. Smith, B. A. Connor, H. I. Karunadasa, *Chem. Rev.* **2019**, *119*, 3104.
[29] J. Zhou, J. Huang, *Adv. Sci.* **2018**, *5*, 1700256.
[30] R. Cheng, C. C. Chung, H. Zhang, F. Liu, W. T. Wang, Z. Zhou, S. Wang, A. B. Djurišić, S. P. Feng, *Adv. Energy Mater.* **2019**, *9*, 1901980.
[31] J. Markus, A. B. McBratney, *Environ. Int.* **2001**, *27*, 399.
[32] F. Li, Y. Wang, K. Xia, R. L. Z. Hoye, V. Pecunia, *J. Mater. Chem. A* **2020**, *8*, 4396.
[33] S. Yeon Park, J.-S. Park, B. Jo Kim, H. Lee, A. Walsh, K. Zhu, D. Hoe Kim, H. Suk Jung, *Nat. Sustainability* **2020**, https://doi.org/10.1038/s41893-020-0586-6.
[34] M. Li, F. Igbari, Z. K. Wang, L. S. Liao, *Adv. Energy Mater.* **2020**, *10*, 2000641.
[35] N. Moody, S. Sesena, D. W. deQuilettes, B. D. Dou, R. Swartwout, J. T. Buchman, A. Johnson, U. Eze, R. Brenes, M. Johnston, C. L. Haynes, V. Bulović, M. G. Bawendi, *Joule* **2020**, *4*, 970.
[36] E. T. Hoke, D. J. Slotcavage, E. R. Dohner, A. R. Bowring, H. I. Karunadasa, M. D. Mcgehee, *Chem. Sci.* **2015**, *6*, 613.
[37] A. Abate, *Joule* **2017**, *1*, 659.
[38] A. Babayigit, A. Ethirajan, M. Muller, B. Conings, *Nat. Mater.* **2016**, *15*, 247.
[39] V. Pecunia, Y. Yuan, J. Zhao, K. Xia, Y. Wang, S. Duhm, L. Portilla, F. Li, *Nano-Micro Lett.* **2020**, *12*, 27.
[40] R. Wang, J. Wang, S. Tan, Y. Duan, Z. K. Wang, Y. Yang, *Trends Chem.* **2019**, *1*, 368.
[41] Q. Zhang, H. Ting, S. Wei, D. Huang, C. Wu, W. Sun, B. Qu, S. Wang, Z. Chen, L. Xiao, *Mater. Today Energy* **2018**, *8*, 157.
[42] R. E. Brandt, V. Stevanović, D. S. Ginley, T. Buonassisi, *MRS Commun.* **2015**, *5*, 265.
[43] R. Mohan, *Nat. Chem.* **2010**, *2*, 336.
[44] A. M. Ganose, C. N. Savory, D. O. Scanlon, *Chem. Commun.* **2017**, *53*, 20.
[45] R. L. Z. Hoye, L. C. Lee, R. C. Kurchin, T. N. Huq, K. H. L. Zhang, M. Sponseller, L. Nienhaus, R. E. Brandt, J. Jean, J. Al Polizzotti, A. Kursumović, M. G. Bawendi, V. Bulović, V. Stevanović, T. Buonassisi, J. L. MacManus-Driscoll, *Adv. Mater.* **2017**, *29*, 1702176.
[46] L. C. Lee, T. N. Huq, J. L. Macmanus-Driscoll, R. L. Z. Hoye, *APL Mater.* **2018**, *6*, 084502.
[47] B. Saparov, F. Hong, J. P. Sun, H. S. Duan, W. Meng, S. Cameron, I. G. Hill, Y. Yan, D. B. Mitzi, *Chem. Mater.* **2015**, *27*, 5622.
[48] F. Umar, J. Zhang, Z. Jin, I. Muhammad, X. Yang, H. Deng, K. Jahangeer, Q. Hu, H. Song, J. Tang, *Adv. Opt. Mater.* **2019**, *7*, 1801368.
[49] A. Singh, K. M. Boopathi, A. Mohapatra, Y. F. Chen, G. Li, C. W. Chu, *ACS Appl. Mater. Interfaces* **2018**, *10*, 2566.
[50] J. P. Correa-Baena, L. Nienhaus, R. C. Kurchin, S. S. Shin, S. Wieghold, N. T. Putri Hartono, M. Layurova, N. D. Klein, J. R. Poindexter, A. Polizzotti, S. Sun, M. G. Bawendi, T. Buonassisi, *Chem. Mater.* **2018**, *30*, 3734.
[51] P. C. Harikesh, H. K. Mulmudi, B. Ghosh, T. W. Goh, Y. T. Teng, K. Thirumal, M. Lockrey, K. Weber, T. M. Koh, S. Li, S. Mhaisalkar, N. Mathews, *Chem. Mater.* **2016**, *28*, 7496.
[52] S. Weber, T. Rath, K. Fellner, R. Fischer, R. Resel, B. Kunert, T. Dimopoulos, A. Steinegger, G. Trimmel, *ACS Appl. Energy Mater.* **2019**, *2*, 539.
[53] H. Gleskova, I.-C. Cheng, S. Wagner, Z. Suo, in *Flexible Electronics*, (Eds: W. S. Wong, A. Salleo), Springer, New York **2009**, Ch. 2.
[54] J. H. Heo, D. S. Lee, D. H. Shin, S. H. Im, *J. Mater. Chem. A* **2019**, *7*, 888.
[55] K. Huang, Y. Peng, Y. Gao, J. Shi, H. Li, X. Mo, H. Huang, Y. Gao, L. Ding, J. Yang, *Adv. Energy Mater.* **2019**, *9*, 1901419.
[56] Y. Peng, F. Li, Y. Wang, Y. Li, R. L. Z. Hoye, L. Feng, K. Xia, V. Pecunia, *Appl. Mater. Today* **2020**, *19*, 100637.
[57] R. A. Jagt, T. N. Huq, K. M. Börsig, D. Sauven, L. C. Lee, J. L. MacManus-Driscoll, R. L. Z. Hoye, *J. Mater. Chem. C* **2020**, *8*, 10791.
[58] T. N. Huq, L. C. Lee, L. Eyre, W. Li, R. A. Jagt, C. Kim, S. Fearn, V. Pecunia, F. Deschler, J. L. MacManus-Driscoll, R. L. Z. Hoye, *Adv. Funct. Mater.* **2020**, *30*, 1909983.
[59] C. C. Boyd, R. C. Shallcross, T. Moot, R. Kerner, L. Bertoluzzi, A. Onno, S. Kavadiya, C. Chosy, E. J. Wolf, J. Werner, J. A. Raiford, C. de Paula, A. F. Palmstrom, Z. J. Yu, J. J. Berry, S. F. Bent, Z. C. Holman, J. M. Luther, E. L. Ratcliff, N. R. Armstrong, M. D. McGehee, *Joule* **2020**, *4*, 1759.
[60] S. C. Liu, Z. Li, Y. Yang, X. Wang, Y. X. Chen, D. J. Xue, J. S. Hu, *J. Am. Chem. Soc.* **2019**, *141*, 18075.
[61] J. He, W. H. Fang, R. Long, *Chem. Sci.* **2019**, *10*, 10079.
[62] M. T. Greiner, M. G. Helander, Z. Wang, W. Tang, Z. Lu, *J. Phys. Chem. C* **2010**, *114*, 19777.
[63] J. Kwon, Y. Takeda, R. Shiwaku, S. Tokito, K. Cho, S. Jung, *Nat. Commun.* **2019**, *10*, 54.
[64] H. Matsui, Y. Takeda, S. Tokito, *Org. Electron.* **2019**, *75*, 105432.
[65] V. Pecunia, M. Nikolka, A. Sou, I. Nasrallah, A. Y. Amin, I. McCulloch, H. Sirringhaus, *Adv. Mater.* **2017**, *29*, 1606938.
[66] V. Pecunia, K. Banger, A. Sou, H. Sirringhaus, *Org. Electron.* **2015**, *21*, 177.
[67] G. Hills, C. Lau, A. Wright, S. Fuller, M. D. Bishop, T. Srimani, P. Kanhaiya, R. Ho, A. Amer, Y. Stein, D. Murphy, A. C. Arvind, M. M. Shulaker, *Nature* **2019**, *572*, 595.
[68] L. Portilla, J. Zhao, W. Yan, L. Sun, F. Li, M. Robin, M. Wei, Z. Cui, L. G. Occhipinti, T. D. Anthopoulos, V. Pecunia, *ACS Nano* **2020**, https://doi.org/10.1021/acsnano.0c06619.
[69] V. Pecunia, M. Fattori, S. Abdinia, H. Sirringhaus, E. Cantatore, *Organic and Amorphous-Metal-Oxide Flexible Analogue Electronics*, Cambridge University Press, Cambridge, UK **2018**.
[70] K. Myny, *Nat. Electron.* **2018**, *1*, 30.
[71] J. S. Heo, J. Eom, Y. H. Kim, S. K. Park, *Small* **2018**, *14*, 1703034.
[72] L. J. A. Koster, V. D. Mihailetchi, R. Ramaker, P. W. M. Blom, *Appl. Phys. Lett.* **2005**, *86*, 123509.
[73] T. S. Sherkar, C. Momblona, L. Gil-Escrig, J. Ávila, M. Sessolo, H. J. Bolink, L. J. A. Koster, *ACS Energy Lett.* **2017**, *2*, 1214.
[74] W. Tress, M. Yavari, K. Domanski, P. Yadav, B. Niesen, J. P. Correa Baena, A. Hagfeldt, M. Graetzel, *Energy Environ. Sci.* **2018**, *11*, 151.
[75] P. Calado, D. Burkitt, J. Yao, J. Troughton, T. M. Watson, M. J. Carnie, A. M. Telford, B. C. O'Regan, J. Nelson, P. R. F. Barnes, *Phys. Rev. Appl.* **2019**, *11*, 044005.
[76] R. H. Blube, *Photoconductivity of Solids*, Wiley, New York **1960**.
[77] W. Shockley, H. J. Queisser, *J. Appl. Phys.* **1961**, *32*, 510.
[78] L. Yu, A. Zunger, *Phys. Rev. Lett.* **2012**, *108*, 068701.
[79] H. Zhu, M. Pan, M. B. Johansson, E. M. J. J. Johansson, *ChemSusChem* **2017**, *10*, 2592.
[80] Q. Zhang, C. Wu, X. Qi, F. Lv, Z. Zhang, Y. Liu, S. Wang, B. Qu, Z. Chen, L. Xiao, *ACS Appl. Energy Mater.* **2019**, *2*, 3651.
[81] J. Chen, J. Qi, R. Liu, X. Zhu, Z. Wan, Q. Zhao, S. Tao, C. Dong, G. Y. Ashebir, W. Chen, R. Peng, F. Zhang, S. Yang, X. Tian, M. Wang, *Commun. Chem.* **2019**, *2*, 121.

[82] Z. Yang, X. Wang, Y. Chen, Z. Zheng, Z. Chen, W. Xu, W. Liu, Y. (Michael) Yang, J. Zhao, T. Chen, H. Zhu, *Nat. Commun.* **2019**, *10*, 4540.
[83] R. Tang, X. Wang, W. Lian, J. Huang, Q. Wei, M. Huang, Y. Yin, C. Jiang, S. Yang, G. Xing, S. Chen, C. Zhu, X. Hao, M. A. Green, T. Chen, *Nat. Energy* **2020**, *5*, 587.
[84] N. Giesbrecht, A. Weis, T. Bein, *J. Phys. Energy* **2020**, *2*, 024007.
[85] W. A. Dunlap-Shohl, I. G. Hill, Y. Yan, D. B. Mitzi, *Chem. Mater.* **2018**, *30*, 8226.
[86] C. Lu, J. Zhang, H. Sun, D. Hou, X. Gan, M. H. Shang, Y. Li, Z. Hu, Y. Zhu, L. Han, *ACS Appl. Energy Mater.* **2018**, *1*, 4485.
[87] B. Ghosh, B. Wu, X. Guo, P. C. Harikesh, R. A. John, T. Baikie, A. T. S. W. Arramel, C. Guet, T. C. Sum, S. Mhaisalkar, N. Mathews, *Adv. Energy Mater.* **2018**, *8*, 1802051.
[88] Y. Liu, J. Zhang, H. Wu, W. Cui, R. Wang, K. Ding, S. Lee, *Nano Energy* **2017**, *34*, 257.
[89] J. C. de Mello, H. F. Wittmann, R. H. Friend, *Adv. Mater.* **1997**, *9*, 230.